

Article

Electro-Oxidation of Ammonia at Novel $\text{Ag}_2\text{O}-\text{PrO}_2/\gamma\text{-Al}_2\text{O}_3$ Catalysts

Mariam Khan ^{1,2}, Naveed Kausar Janjua ^{2,*}, Safia Khan ² , Ibrahim Qazi ³, Shafaqat Ali ^{4,5} and Tahani Saad Algarni ⁶ 

- ¹ School of Applied Sciences and Humanity, National University of Technology, Islamabad 44000, Pakistan; mariamkhan@nutech.edu.pk
² Department of Chemistry, Quaid-i-Azam University, Islamabad 45320, Pakistan; safiakhan@chem.qau.edu.pk
³ Department of Materials Science and Engineering, Institute of Space Technology, Islamabad 44000, Pakistan; ibrahim.qazi@ist.edu.pk
⁴ Department of Environmental Science and Engineering, Government College University, Faisalabad 38000, Pakistan; shafaqataligill@yahoo.com
⁵ Department of Biological Sciences and Technology, China Medical University, Taichung 40402, Taiwan
⁶ Chemistry Department, College of Science, King Saud University, Riyadh 11451, Saudi Arabia; tahanis@ksu.edu.sa
 * Correspondence: nkjanjua@qau.edu.pk

Abstract: An $\text{Ag}_2\text{O}_{(x)}-\text{PrO}_{2(y)}/\gamma\text{-Al}_2\text{O}_3$ electrocatalyst series ($X:Y$ is for $\text{Ag}:\text{Pr}$ from 0 to 10) was synthesized, to use synthesized samples in electrochemical applications, a step in fuel cells advancements. $\text{Ag}_2\text{O}_{(x)}-\text{PrO}_{2(y)}/\gamma\text{-Al}_2\text{O}_3/\text{Glassy-Carbon}$ was investigated for electrochemical oxidation of ammonia in alkaline medium and proved to be highly effective, having high potential utility, as compared to commonly used Pt-based electrocatalysts. In this study, gamma alumina as catalytic support was synthesized via precipitation method, and stoichiometric wt/wt.% compositions of $\text{Ag}_2\text{O}-\text{PrO}_2$ were loaded on $\gamma\text{-Al}_2\text{O}_3$ by co-impregnation method. The desired phase of $\gamma\text{-Al}_2\text{O}_3$ and supported nanocatalysts was obtained after heat treatment at 800 and 600 °C, respectively. The successful loadings of $\text{Ag}_2\text{O}-\text{PrO}_2$ nanocatalysts on surface of $\gamma\text{-Al}_2\text{O}_3$ was determined by X-rays diffraction (XRD), Fourier-transform Infrared Spectroscopy (FTIR), and energy dispersive analysis (EDX). The nano-sized domain of the sample powders sustained with particle sizes was calculated via XRD and scanning electron microscopy (SEM). The surface morphology and elemental compositions were examined by SEM, transmission electron microscopy (TEM) and EDX. The conductive and electron-transferring nature was investigated by cyclic voltammetry and electrochemical impedance (EIS). Cyclic voltammetric profiles were observed, and respective kinetic and thermodynamic parameters were calculated, which showed that these synthesized materials are potential catalysts for ammonia electro-oxidation. $\text{Ag}_2\text{O}_{(6)}-\text{PrO}_{2(4)}/\gamma\text{-Al}_2\text{O}_3$ proved to be the most proficient catalyst among all the members of the series, having greater diffusion coefficient, heterogeneous rate constant and lesser Gibbs free energy for this system. The catalytic activity of these electrocatalysts is revealed from electrochemical studies which reflected their potentiality as electrode material in direct ammonia fuel cell technology for energy production.

Keywords: ammonia electro-oxidation; cyclic voltammetry; electrochemical surface area (ECSA); electrocatalysts; nanocomposites



Citation: Khan, M.; Janjua, N.K.; Khan, S.; Qazi, I.; Ali, S.; Saad Algarni, T. Electro-Oxidation of Ammonia at Novel $\text{Ag}_2\text{O}-\text{PrO}_2/\gamma\text{-Al}_2\text{O}_3$ Catalysts. *Coatings* **2021**, *11*, 257. <https://doi.org/10.3390/coatings11020257>

Received: 25 January 2021
 Accepted: 11 February 2021
 Published: 22 February 2021

Publisher's Note: MDPI stays neutral with regard to jurisdictional claims in published maps and institutional affiliations.



Copyright: © 2021 by the authors. Licensee MDPI, Basel, Switzerland. This article is an open access article distributed under the terms and conditions of the Creative Commons Attribution (CC BY) license (<https://creativecommons.org/licenses/by/4.0/>).

1. Introduction

Energy generation from hydrogen in a sustainable and continuous manner is the foremost concern of scientists and engineers across the globe [1,2]. Fuel cells are considered to be a great contributor of energy production which changes the chemical energy to electrical energy through an electrochemical reaction in the cell [3–5]. Among several fuel cells, the ammonia fuel cell is a better substitute of carbon-based conventional energy

generating technologies [6,7]. Liquid ammonia is a promising hydrogen carrier, owing to its favorable properties, like high storage capacity, hydrogen density (17.8 wt.%, 10.7 kg H₂/100 L at 1 MPa and 298 K), carbon free fuel, high boiling point and odor; thus, the challenges associated with storage of hydrogen can be overcome [8]. Volumetric hydrogen density of ammonia is 1.5 times higher than pure hydrogen, because ammonia is effortlessly liquefiable at room temperature and 1 MPa [9]. Moreover, ammonia-derived electricity is under constant research for running gas turbines, steam turbines and alkaline fuel cells, which are being commercialized at lower-scale off-grid power plants [10,11]. However, the larger-scale implementation of ammonia fuel cells is currently hindered due to less efficient and much expensive electrodes [12]. A variety of electrode materials are being investigated for ammonia electro-oxidation in basic conditions [13–15]. Although Pt and Pt based materials are being employed as electrodes in ammonia fuel cells, due to sufficient catalytic significance, their industrial-scale applications still encounter critical challenges due to non-affordability [16,17]. Hence, development of novel Pt free cheaper electrodes is required as an alternative to accelerate ammonia fuel cells in energy generating technology [17]. Moreover, multiple factors affect the catalytic performance of electrodes towards ammonia electro-oxidation, including the nature of the support material and modifiers/promotor, as well as the synthesis conditions [18,19].

Gamma alumina (γ -Al₂O₃) is a highly used catalyst support, owing to its worthy mechanical properties, high thermal stability and ability to disperse the active oxide precursors [20,21]. Moreover, the introduction of metal oxides into γ -Al₂O₃ support is found to promote the catalyst's efficiency towards electro-oxidation processes [22–24]. With this intent, Ag₂O is used as a catalyst promotor in several oxidation processes [25,26]. Furthermore, lanthanide and lanthanide oxides seemed to be efficient promotors, exhibiting enhanced catalytic activity in many electro-oxidation processes [20]. Therefore, catalytic materials based on praseodymium oxide and praseodymium containing mixed metal oxides of high-surface area also provide efficient energy production [27]. Moreover, mixed metal oxides, including sieves supported metal oxides and bulk mixed metal oxides, have experienced an intense paradigm in electrocatalysis over the past few years [28–30].

Herein, a series of novel mixed metal oxides Ag₂O–PrO₂/ γ -Al₂O₃ electrocatalysts were prepared by an incipient wet impregnation method. The aim of present research was to observe the effect of variation in percentage composition of PrO₂ and Ag₂O supported on γ -Al₂O₃ towards ammonia electro-oxidation. Physical and electrochemical properties of as-synthesized catalysts were investigated for NH₃ electro-oxidation via different techniques, i.e., XRD, FTIR, SEM, EDS, EIS and cyclic voltammetry. Figure 1 shows the schematic diagram for experimental procedure of electro-oxidation of ammonia over as synthesized electrocatalysts.

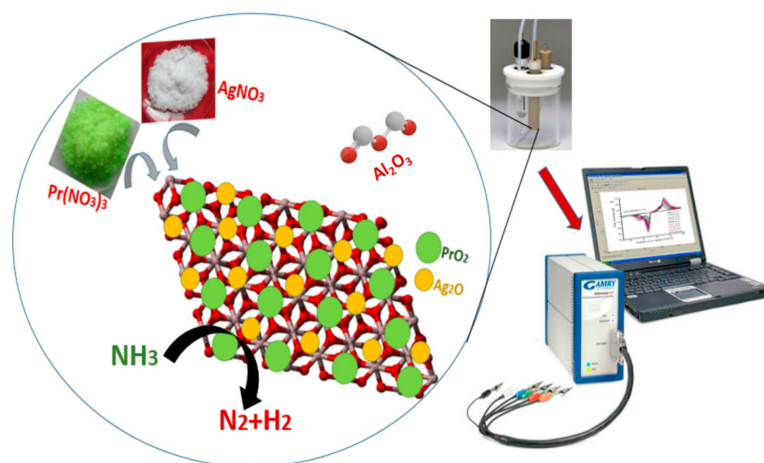


Figure 1. Graphical abstract elucidating the experimental, mechanistic and electrochemical insight.

2. Catalyst Preparation

2.1. Materials

Chemicals used for synthesis were bought from Sigma Aldrich (St. Louis, MO, USA). The chemicals used for the present work are aluminum nitrate ($\text{Al}(\text{NO}_3)_3 \cdot 9\text{H}_2\text{O}$), ammonia solution (NH_3), praseodymium nitrate hexahydrate ($\text{Pr}(\text{NO}_3)_3 \cdot 6\text{H}_2\text{O}$), silver nitrate (AgNO_3), potassium hydroxide (KOH), sulfur acid (H_2SO_4), potassium hexacyanoferrate (III) ($\text{K}_4[\text{Fe}(\text{CN})_6]$), alumina powder and Nafion.

2.2. Synthesis of $\gamma\text{-Al}_2\text{O}_3$

In total, a 1 M solution of aluminum nitrate nonahydrate and a 3 M ammonia solution were prepared in deionized water. The ammonia solution was added dropwise into precursor solution, under constant stirring until formation of homogeneous precipitates of aluminum hydroxide. The temperature of solution was maintained at 60 °C. White gelatinous $\text{Al}(\text{OH})_3$ precipitates were formed and were kept on heating, until semi-solid material was formed. The precipitates were dried at 200 °C overnight. The $\text{Al}(\text{OH})_3$ precipitates were calcined at 800 °C, to form γ -alumina, for 2 h. The calcined sample was grinded with acetone, to form powdered γ -alumina.

2.3. Synthesis of $\text{Ag}_2\text{O-PrO}_2/\gamma\text{-Al}_2\text{O}_3$

The metal oxides composites catalysts were prepared via co-impregnation method. In this method, the solution of active element precursors was mixed before impregnating on support. We used an adapted method to synthesize the wt/wt.% alumina supported composites of silver and praseodymium oxides. Stoichiometric amounts of γ -alumina were taken and wetted with requisite volume of praseodymium nitrate hexahydrate 0.5 M and silver nitrate 0.5 M to load wt/wt.% Ag-Pr oxides. The mixtures were soaked overnight, evaporated and dried at 100 °C. The dried samples were calcined at 600 °C, for 2 h, and finely ground to $\text{Ag}_2\text{O-PrO}_2/\gamma\text{-Al}_2\text{O}_3$ catalysts.

3. Physical Characterization

3.1. X-Ray Diffraction Analysis

The size and phase of all synthesized materials ($\text{Ag}_2\text{O}_{(X)}\text{-PrO}_{2(\gamma)}/\gamma\text{-Al}_2\text{O}_3$) were examined by X-ray diffraction using (PANalytical X'PERT High Score's diffractometer, Malvern, UK), exhibiting Cu K_α radiation, works in the range of (10°–80°) Figure 2a,b. The peaks observed at 2θ of 37.0°, 40.20°, 45.78°, 61.30° and 66.99° were assigned to 311, 222, 400, 511 and 440 crystal planes. These are according to JCPDS (Joint Committee on Powder Diffraction Standards) card no. (29-0063) [31,32]. The gamma phase of synthesized alumina calcined at 800 °C is suggested by these peak positions. The XRD corroborate the characteristic peaks of Ag_2O (26.78°, 32.14°, 38.04° and 67.48°), PrO_2 (28.1°, 46.7°, 55.6° and 78.2°) and $\gamma\text{-Al}_2\text{O}_3$, which are related to JCPDS card no. (76-1393), (24-1006) and (29-0063), respectively [33,34]. The diffraction peaks at 67.48° are indexed to (222) planes of face-centered cubic silver oxide [35]. These peaks correspond to the successful loadings of promoting metal oxides on surface of support. Crystallinity of the catalysts increases with increasing the contents of silver oxide precursor on the $\gamma\text{-Al}_2\text{O}_3$ support as sharper peaks are observed with higher loadings of Ag_2O . No phase segregation is observed as obvious from XRD patterns.

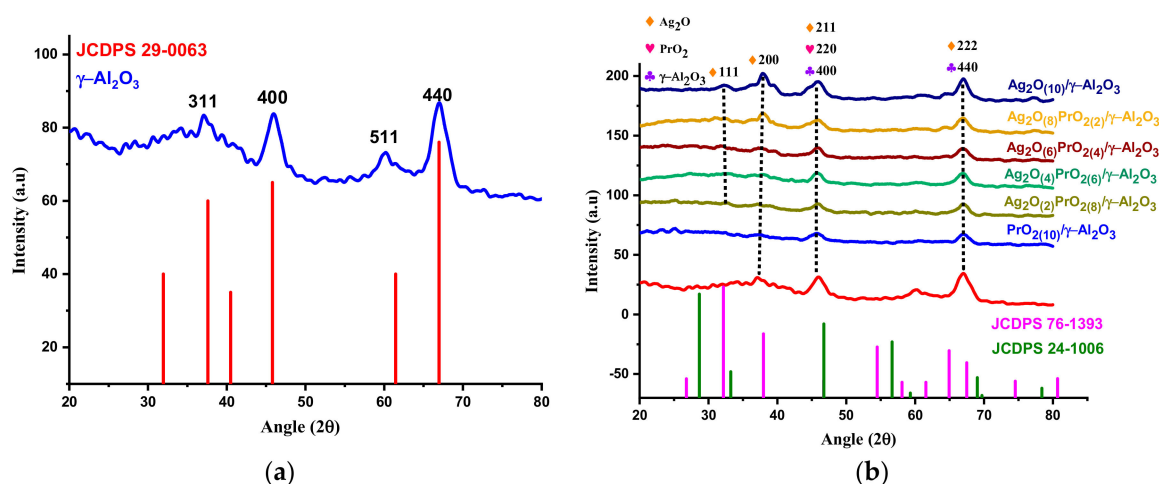


Figure 2. X-ray diffraction peaks of (a) γ - Al_2O_3 with Joint Committee on Powder Diffraction Standards (JCPDS) card numbers. (b) Overlay of XRD peaks of γ - Al_2O_3 and $\text{Ag}_2\text{O}_{(x)}\text{-PrO}_{2(y)}/\gamma\text{-Al}_2\text{O}_3$, along with JCPDS card numbers.

The average crystallite sizes (D_{avg}), which are enlisted in Table 1, were calculated by the Scherrer equation [36]:

$$D_{\text{avg}} \text{ (nm)} = 57.2k\lambda / \beta \cos\theta \quad (1)$$

where D_{avg} is the average crystallite size, constant k is shape factor (0.9), λ is the wavelength (0.154 nm), β corresponds to the peak width at half maximum intensity and θ is the peak position. D_{avg} for support (γ - Al_2O_3) is 18.3 nm, while for nanomaterials, it lies in the range of 25–42 nm.

Table 1. Calculated values for average crystallite size and average particle size.

Electrocatalysts	$D_{\text{avg}}(\text{XRD})$ (nm)	$D_{\text{avg}}(\text{SEM})$ (nm)
$\text{PrO}_{2(10)}/\gamma\text{-Al}_2\text{O}_3$	41.3	26.02
$\text{Ag}_2\text{O}_{(2)}\text{-PrO}_{2(8)}/\gamma\text{-Al}_2\text{O}_3$	25.4	20.76
$\text{Ag}_2\text{O}_{(4)}\text{-PrO}_{2(6)}/\gamma\text{-Al}_2\text{O}_3$	28.9	29.41
$\text{Ag}_2\text{O}_{(6)}\text{-PrO}_{2(4)}/\gamma\text{-Al}_2\text{O}_3$	32.3	31.01
$\text{Ag}_2\text{O}_{(8)}\text{-PrO}_{2(2)}/\gamma\text{-Al}_2\text{O}_3$	20.3	23.02
$\text{Ag}_2\text{O}_{(10)}/\gamma\text{-Al}_2\text{O}_3$	25.0	31.04

3.2. FTIR Analysis

The Fourier-transform infrared spectroscopy (FTIR) spectra for γ - Al_2O_3 and all synthesized nanocomposites inserted in KBr powder system were investigated in wavelength range (400–4000) cm^{-1} by using Nicolet 5PC, Nicolet Analytical Instrument (Protea, Cambridgeshire, UK, Figure 3). The vibration bands observed in the range of (3500–4000) cm^{-1} correspond to O–H stretching vibrations. These bands appeared because of moisture absorbed by the samples [37]. C–O vibration bands due to adsorbed CO_2 also appeared in the range of (1500–2500) cm^{-1} [38]. The metal oxides vibration bands are seen between 300 and 700 cm^{-1} [39]. The bands in Figure 3b represent the stretching and bending vibration modes of Ag_2O [40] and stretching vibration bands of PrO_2 [41].

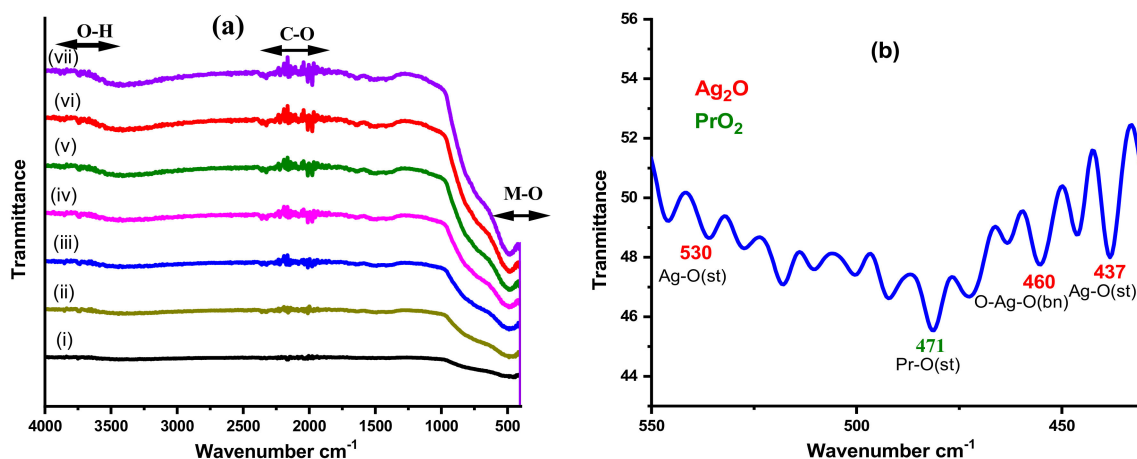


Figure 3. (a) FTIR spectra of γ - Al_2O_3 and $\text{Ag}_2\text{O}_{(x)}\text{-PrO}_{2(y)}/\gamma\text{-Al}_2\text{O}_3$ nanomaterials. (b) FTIR spectrum representing vibration modes of Ag-O and Pr-O bonds.

3.3. SEM, TEM and EDX Analysis

Surface structure investigation of the nanomaterials was evaluated via scanning electron microscopy (SEM), armed with energy dispersive analysis (EDX), by using MIRA3 TESCAN (Brno, Czech Republic) microscope and transmission electron microscopy (TEM, Thermofisher, Manchester, UK). The SEM images for synthesized nanocomposites are given in figures on different scales. In Figure 4A, the first SEM micrograph corresponds to pure $\gamma\text{-Al}_2\text{O}_3$, which appeared to be like a plate-like interconnected network, which, upon impregnation, converted to globular structures. From Figure 4B, it is clear that there is no segregation of phase, which substantiates that metal oxide precursors are homogeneously dispersed on surface of support. The average particle size from these SEM micrographs was estimated by using the ImageJ software (Version: 1.52v) and is tabulated in Table 1. Figure 4D represents the distributions of diameters of nanoparticles ($\text{Ag}_2\text{O}_{(6)}\text{-PrO}_{2(4)}/\gamma\text{-Al}_2\text{O}_3$) via histograms presenting the D_{avg} . The estimated average particle sizes from SEM are also in dimensions and slightly in accordance with that calculated by XRD. Figure 4C,D represents the EDX spectra of $\text{Ag}_2\text{O}_{(4)}\text{-PrO}_{2(6)}/\gamma\text{-Al}_2\text{O}_3$ composition which confirms the presence of desired components in synthesized nanomaterial. These EDX analyses are in accordance with XRD, as we have not seen any extra peak in XRD diffraction pattern. The wt/wt.% elemental composition of all supported nanocomposites is given in Table 2.

The Transmission Electron Microscopy (TEM) analysis in Figure 4F showed that nanocomposites are in good contact with the surface of support and have nanosized morphology also shown by SEM micrographs. The TEM images supported the agreement that particles are closed spheres with a smooth surface and are uniform in size. There is a low contrast shell around them that is attributed to the layer of silver oxides [42]. The histogram in inset (b) of Figure 4F describes the distribution of nanoparticles presenting the synthesized materials that are nanosized, and inset (a) describes the area of TEM micrograph where distributions of particles are taken.

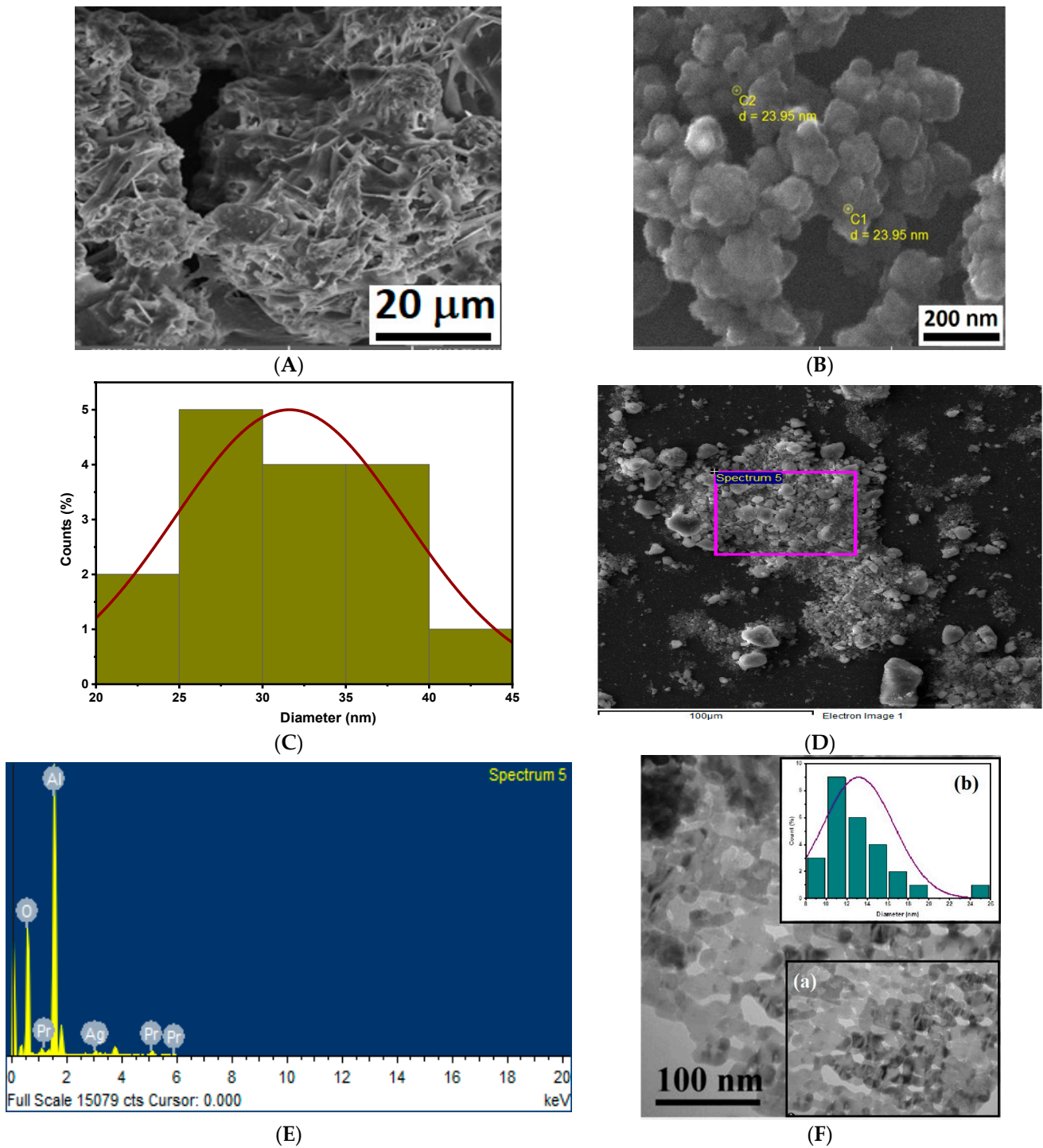


Figure 4. SEM micrographs for (A) Al_2O_3 and (B) $\text{Ag}_2\text{O}_{(10)}/\gamma\text{-Al}_2\text{O}_3$ nanocatalysts. (C) Particle size distribution of $\text{Ag}_2\text{O}_{(6)}\text{-PrO}_{2(4)}/\gamma\text{-Al}_2\text{O}_3$. (D,E) EDX spectrum of $\text{Ag}_2\text{O}_{(4)}\text{-PrO}_{2(6)}/\gamma\text{-Al}_2\text{O}_3$ composition. (F) TEM analysis of sample $\text{Ag}_2\text{O}_{(2)}\text{-PrO}_{2(8)}/\gamma\text{-Al}_2\text{O}_3$, the inset (a) describes the area where distribution of particles taken and inset (b) represents the distributions of particles.

Table 2. Elemental compositions (wt.%) from EDX analysis of samples.

Samples	wt.% Al	wt.% O	wt.% Pr	wt.% Ag
PrO ₂₍₁₀₎ /γ-Al ₂ O ₃	26.90	69.90	9.20	–
Ag ₂ O ₍₂₎ -PrO ₂₍₈₎ /γ-Al ₂ O ₃	42.40	48.86	8.19	1.56
Ag ₂ O ₍₄₎ -PrO ₂₍₆₎ /γ-Al ₂ O ₃	42.57	51.88	5.87	3.45
Ag ₂ O ₍₆₎ -PrO ₂₍₄₎ /γ-Al ₂ O ₃	38.70	57.76	3.54	6.30
Ag ₂ O ₍₈₎ -PrO ₂₍₂₎ /γ-Al ₂ O ₃	35.24	61.00	1.54	7.39
Ag ₂ O ₍₁₀₎ /γ-Al ₂ O ₃	32.95	64.36	–	8.95

4. Electrochemical Characterization

An electrochemical study of the as-prepared electrocatalysts was performed, using Gamry potentiostat interface 1000 (Gamry, Warminster, PA, USA). A three-electrode system was established by modifying glassy carbon (GC) as working electrode, platinum wire as counter electrode and Ag/AgCl (3 M KCl) as reference electrode. The glassy carbon (GC) electrode was first polished by using alumina slurry and then cleaned with ethanol, prior to pouring the catalyst ink prepared in ethanol, and a solution of 5% Nafion (2.0 μL) was added to catalyst, to bind the powder catalyst at the GC surface. We used 5% Nafion as binders, as it has greater stability over others polymer. It also helps in the passivation of surface from by-products formed during reactions, to protect the catalyst from chemical attack [43].

4.1. Estimation of Electrochemical Surface Area (ECSA) of As-Synthesized Electrocatalysts

Electrochemical active surface area (ECSA) of Ag₂O-PrO₂/γ-Al₂O₃ samples was estimated by cyclic voltammetric profile, using a redox couple having 5 mM potassium ferrocyanide in 3 M KCl, as shown in Figure 5a. The peak current responses at various scan rates are plotted against $v^{1/2}$, applying the Randles-Ševčík equation [44]:

$$I_p = 2.69 \times 10^5 \cdot n^{3/2} \cdot A \cdot (D^0)^{1/2} \cdot v^{1/2} \cdot C \quad (2)$$

where, A is ECSA (cm²); I_p is peak current (μA); n represents the number of electrons transferred (1 in this case); D^0 is the diffusion co-efficient, which is 0.76×10^{-5} cm²·s⁻¹ at standard temperature and pressure (S.T.P); and C is the concentration of K₄[Fe(CN)₆]. Corresponding ECSA values are calculated from slope, and the comparative ECSA for the whole series is presented in Figure 5b. The Ag₂O₍₆₎-PrO₂₍₄₎/γ-Al₂O₃ modified electrode has a greater ECSA value, as compared to other modified electrodes, which means this composition provides greater surface area to catalyze the respective reaction on its surface and facilitates the reaction more efficiently.

4.2. Electrochemical Impedance Spectroscopy EIS

The electron transfer capacities of all modified electrodes were inspected via EIS with Fe²⁺/Fe³⁺ system in 0.1 M KOH. The Nyquist plots observed for Ag₂O_(x)-PrO_{2(y)}/γ-Al₂O₃ modified electrodes are presented in Figure 6, and respective EIS parameters are tabulated in Table 3. The electron transfer resistance systematically reduced from composition (Ag:Pr 0:10) to (Ag:Pr 6:4), and then it increased with increase of Ag content, which endorses that 6:4 wt.% ratio of Ag₂O and PrO₂ on alumina surface is optimum for electrochemical applications. The low value of R_{ct} reflects the greater conductivity and electrocatalytic activity of Ag₂O₍₆₎-PrO₂₍₄₎/γ-Al₂O₃, as compared to other compositions. The variation in electrochemical behavior of all modified electrodes is due to relative ease in electron transferring, which reveals that nanocatalysts are well dispersed on the alumina surface, in the case of Ag₂O₍₆₎-PrO₂₍₄₎/γ-Al₂O₃, as compared to the other compositions.

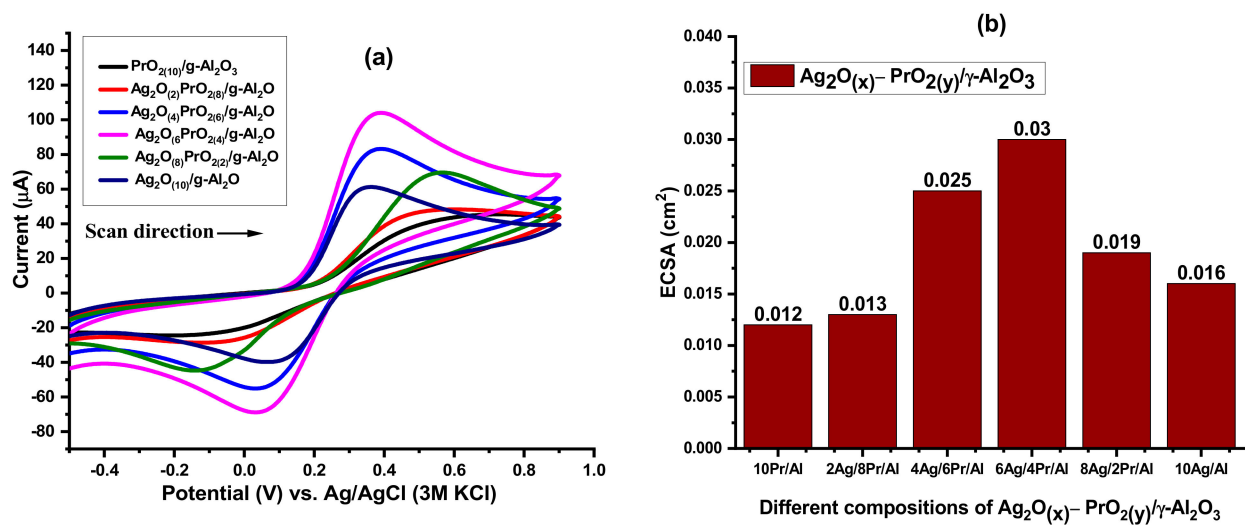


Figure 5. (a) Cyclic voltammograms for $\text{Ag}_2\text{O}(x)\text{-PrO}_2(y)/\gamma\text{-Al}_2\text{O}_3$ in $\text{K}_4[\text{Fe}(\text{CN})_6] + 3 \text{ M KCl}$ redox solution. (b) Bar graph presenting the variation of electrochemical surface area (ECSA) with composition of catalysts.

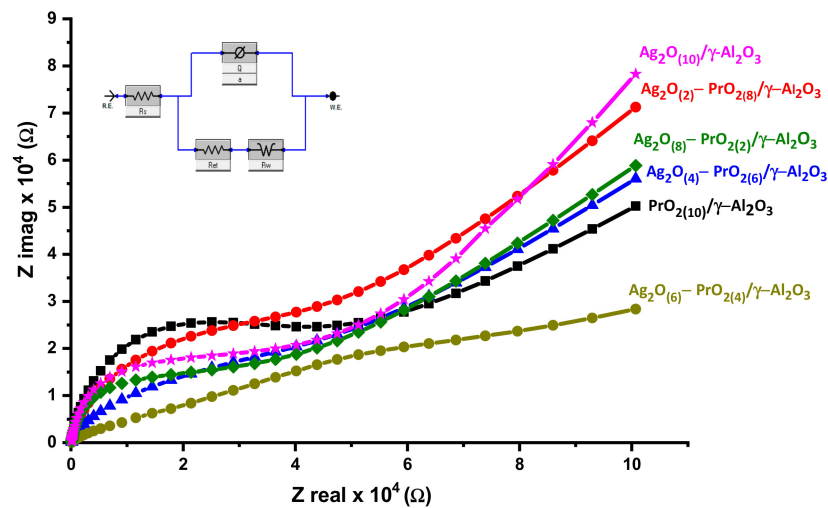


Figure 6. Nyquist plots of $\text{Ag}_2\text{O}(x)\text{-PrO}_2(y)/\gamma\text{-Al}_2\text{O}_3$ modified electrodes recorded in $5 \text{ mM K}_4[\text{Fe}(\text{CN})_6] + 3 \text{ M KCl}$. Inset represents the equivalent circuit.

Table 3. Parameters corresponding to electrochemical impedance (EIS) response of electrocatalysts.

Electrocatalysts	R_s (Ω)	R_{ct} ($\text{k}\Omega$)	CPE (μF)	A	R_w (Ω)	$k_{app}/10^{-9}$ ($\text{cm}\cdot\text{s}^{-1}$)
$\text{PrO}_{2(10)}/\gamma\text{-Al}_2\text{O}_3$	390.0	50.0	3.70	0.90	24.0	1.10
$\text{Ag}_2\text{O}_{(2)}/\text{PrO}_{2(8)}/\gamma\text{-Al}_2\text{O}_3$	389.0	40.4	3.00	0.89	29.0	1.30
$\text{Ag}_2\text{O}_{(4)}/\text{PrO}_{2(6)}/\gamma\text{-Al}_2\text{O}_3$	388.0	27.0	1.40	0.90	24.4	1.97
$\text{Ag}_2\text{O}_{(6)}/\text{PrO}_{2(4)}/\gamma\text{-Al}_2\text{O}_3$	243.0	24.7	43.0	0.90	21.9	2.20
$\text{Ag}_2\text{O}_{(8)}/\text{PrO}_{2(2)}/\gamma\text{-Al}_2\text{O}_3$	388.2	29.7	2.00	0.85	25.6	1.80
$\text{Ag}_2\text{O}_{(10)}/\gamma\text{-Al}_2\text{O}_3$	388.3	36.5	2.20	0.92	29.7	1.50

The modification of electrodes has no effect on solution resistance (R_s) and Warburg resistance (R_w), as these are characteristics of electrolyte solution and diffusion of electroactive specie (which are the same in all measurements), while charge transfer resistance (R_{ct}) and constant phase element (CPE) are affected by modification of electrodes, because these are related to conductive properties of the active material. CPE constitutes two elements, and Q and α represent capacitance and surface roughness, respectively. The value of α varies from 0 to 1 [45]. The modified electrode systems have α value ranging from 0.85 to 0.92, revealing that catalysts show fair surface roughness, which agrees with the SEM results. The electron transfer rate constant for all modified system was calculated by Equation (3) [46].

$$k_{app} = RT/F^2 \cdot R_{ct} \cdot C \quad (3)$$

Where k_{app} is electron transfer rate constant, F is Faraday's constant and R is universal constant in SI units.

It can be seen from Table 2 that the value of electron transfer rate constant for $Ag_2O_{(6)}-PrO_{2(4)}/\gamma-Al_2O_3$ is higher than the other series materials, showing its higher capacity to facilitate the reaction.

5. Results and Discussion

5.1. Ammonia Electro-Oxidation at $Ag_2O_{(x)}-PrO_{2(y)}/\gamma-Al_2O_3$ Modified GC Electrodes

As-synthesized nanocomposites $Ag_2O_{(x)}-PrO_{2(y)}/\gamma-Al_2O_3$ were investigated to check their activities towards the oxidation of NH_3 in alkaline medium. The potential window for ammonia oxidation was from -0.3 to 0.6 mV, in forward and reverse scan. When ammonia oxidation was carried out on modified electrodes at room temperature, two anodic peaks were observed which are related to adsorption/oxidation of ammonia in positive going scan (I and II) Figure 7a. A strong cathodic peak (III) is observed at around 0.05 volts, in the absence (pink curve) and presence (green curve) of ammonia, which is the reduction peak of silver oxide converted into metallic silver [47,48]. An anodic shoulder peak (I) appearing at $0.23-0.27$ V is due to the oxidation of pre-adsorbed hydrogen/nitrogen-containing intermediates species at the surface of modified electrode, which shows the structural sensitivity of nanocatalysts for these adsorbed species [49,50]. There is appearance of cathodic shoulder peak (IV) in ammonia oxidation catalyzed on the surface of higher members of synthesized series (Figure 8c,d), which is due to desorption of hydrogen on the surface [50]. With higher scan rates, the anodic and cathodic shoulder peaks diminished. The onset potential for ammonia oxidation is 0.03 V vs. Ag/AgCl (i.e., 0.023 V vs. NHE approximately) on the surface of modified electrodes and the oxidation peak appear in the range of $0.32-0.51$ volts, which is a low input potential range, as compared to reported systems illustrated in Table 4, in the same medium.

The cyclic voltammetric response of bare glassy carbon and $\gamma-Al_2O_3/GC$ with (red curve) and without (black curve) Ag_2O-PrO_2 loadings was studied in a 5 mM $NH_3 + 0.1$ M KOH system, as shown in Figure 7b,c. The electrochemical oxidation of ammonia in KOH is not observed on bare glassy carbon and $\gamma-Al_2O_3/GC$, while the peak appeared on $Ag_2O_{(x)}-PrO_{2(y)}/\gamma-Al_2O_3/GC$, confirming the electrocatalytic response of $Ag_2O-PrO_2/\gamma-Al_2O_3$ towards the electrochemical oxidation of ammonia, as elucidated by Figure 7b,c.

Table 4. Comparison of oxidation potentials for different systems.

Sr. No.	Modified Electrode Systems	Oxidation Potential Range (V)	Reference
1	Carbon-supported Pt/HOPG electrode	0.55–0.75	[51]
2	Pt film electrode/Si prism	0.45–0.85	[52]
3	Pt disk electrode and Pt/PBI/MWNT	0.45–0.90	[53]
4	Ag–Pr/Al/GC electrode	0.32–0.51	This work

GC, glassy carbon.

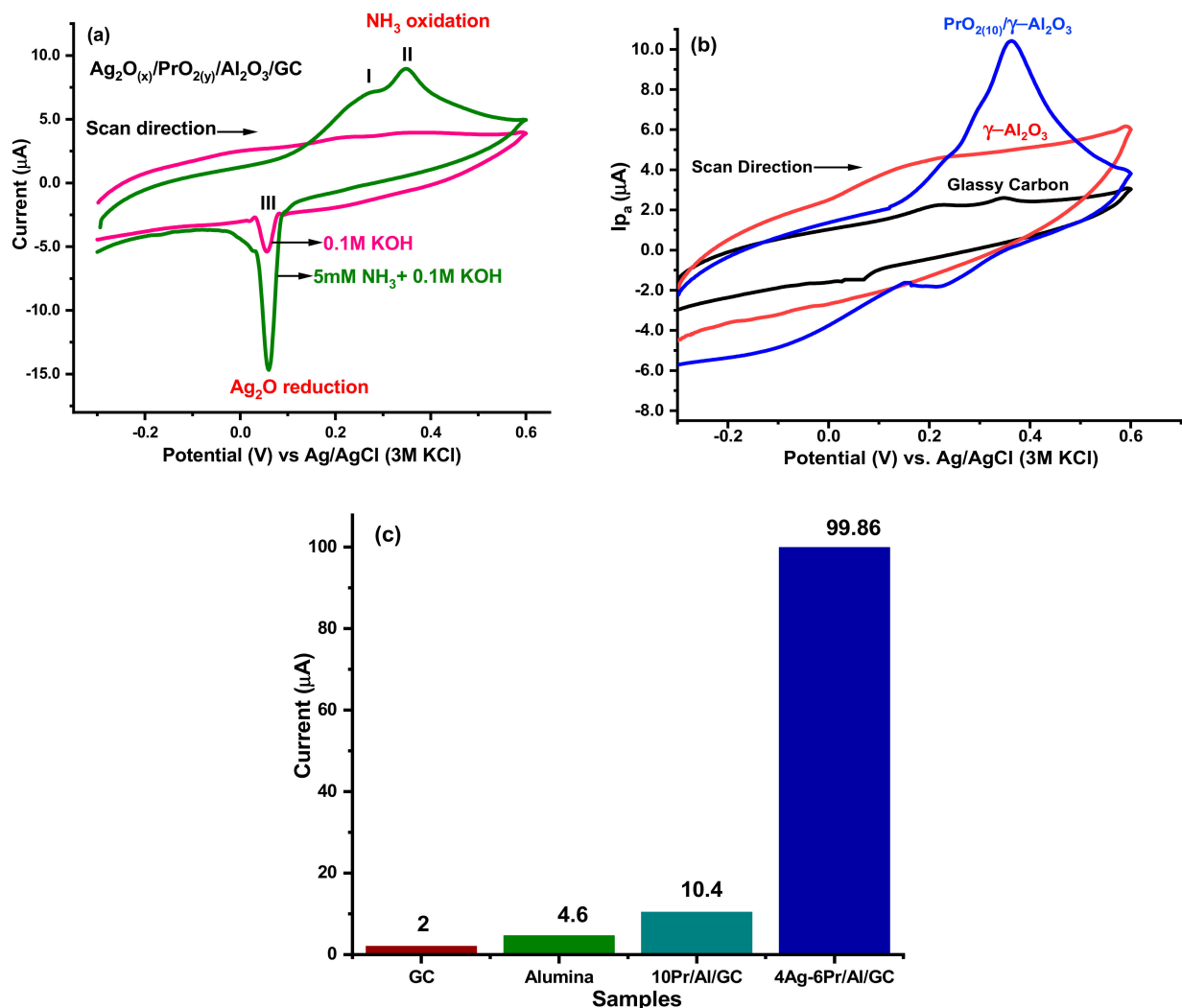


Figure 7. (a) Electrochemical responses and peak position in 0.1 M KOH and 5 mM NH_3 . (b) Cyclic voltammograms towards ammonia oxidation over the surface of bare glassy carbon, $\gamma\text{-Al}_2\text{O}_3$ and $\text{PrO}_{2(10)}/\gamma\text{-Al}_2\text{O}_3$ modified electrodes 0.1 M KOH and 5 mM NH_3 . (c) Comparative peak current response for bare GC, $\gamma\text{-Al}_2\text{O}_3$, and lowest and optimal composition, respectively.

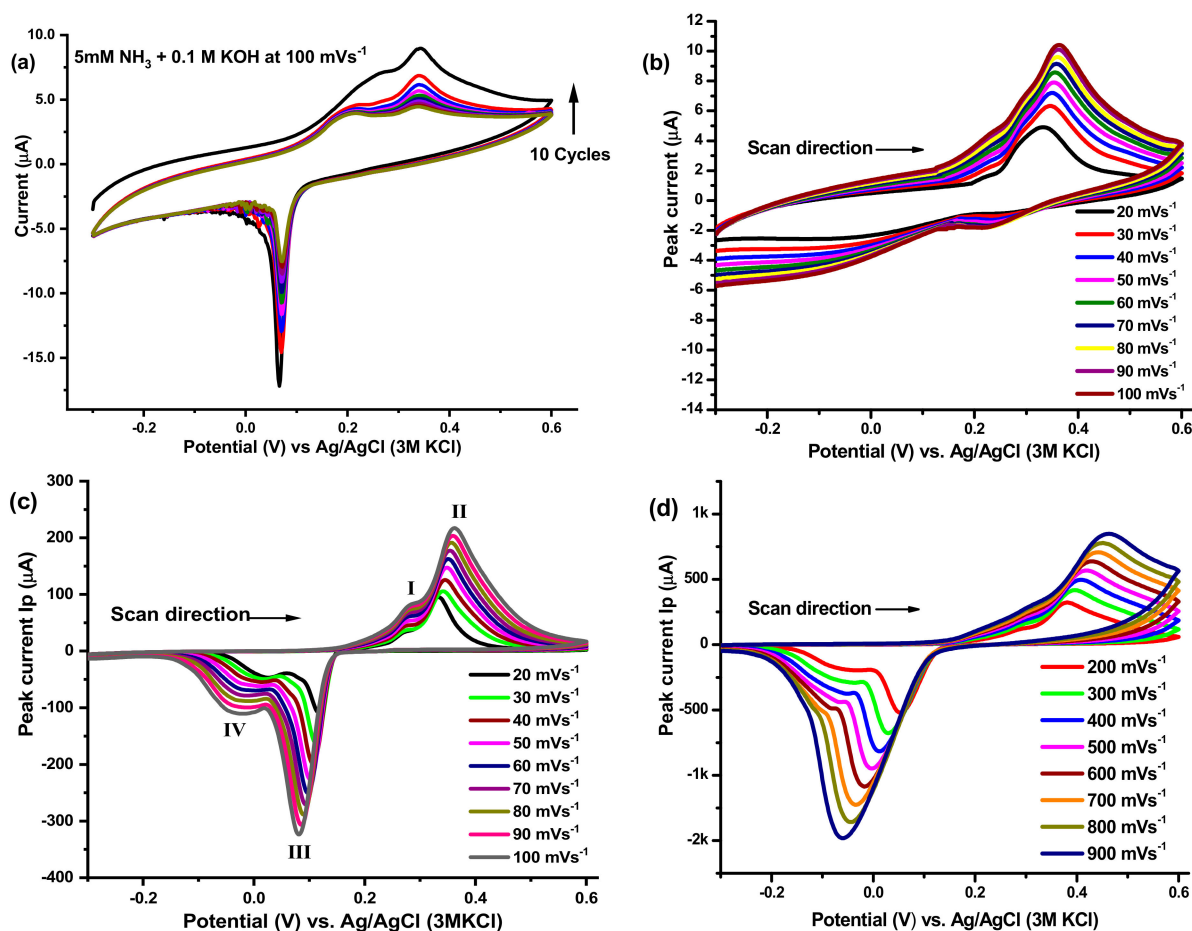


Figure 8. (a) Ten cycles in 5m mM NH_3 + 0.1M KOH at $\text{Ag}_2\text{O}_{(2)}\text{-PrO}_{2(8)}/\gamma\text{-Al}_2\text{O}_3/\text{GC}$. Scan rate variation for (b) $\text{PrO}_{2(10)}/\gamma\text{-Al}_2\text{O}_3$, (c) $\text{Ag}_2\text{O}_{(6)}\text{-PrO}_{2(4)}/\gamma\text{-Al}_2\text{O}_3$ at low scan rates and (d) $\text{Ag}_2\text{O}_{(6)}\text{-PrO}_{2(4)}/\gamma\text{-Al}_2\text{O}_3$, at high scan rates.

For commercialization of electrocatalysts, it is essential to check the electrochemical stability of catalysts; for this purpose, multiple scans have been observed at the surface of modified electrode in 5 mM NH_3 + 0.1 M KOH. The current became constant, and no further decrease was observed, which shows the stability of modified electrode in the system (Figure 8a). The ammonia oxidation was observed at different scan rates on modified GC electrode and is given in Figure 8b–d. Figure 8b tells about the redox behavior of $\text{PrO}_{2(10)}/\gamma\text{-Al}_2\text{O}_3$ response towards ammonia electro-oxidation. It is revealed from the scan rate effect for all the electrochemical systems that the current increases with the increase of scan rate, and the peak potential is shifted towards more a positive potential region. A linear increase in peak current of ammonia oxidation is observed with sweep rate that specifies facilitation of electron transfer process of ammonia electro-oxidation; therefore, as-synthesized nanocatalysts behave like the adsorptive species on the surface of glassy carbon [54]. Figure 8c,d represents the voltammetric behavior of $\text{Ag}_2\text{O}_{(6)}\text{-PrO}_{2(4)}/\gamma\text{-Al}_2\text{O}_3$ at lower and higher scan rates, from which it is seen that separation in positive and negative peak potentials is smaller at low scan rate values, i.e., 20 to 100 mV^{-1} ; hence, it is assumed that the facilitation of ammonia oxidation on surface of all catalysts is more manifested at the lower scan rates. Figure 8c,d shows the peak current dependence upon scan rate, which elaborates that the process of ammonia electro-oxidation over as-proposed catalysts is a diffusion-controlled reaction. Moreover, Figure 9a,b expresses the comparative peak current output of all compositions at lower and higher scan rates, which shows that $\text{Ag}_2\text{O}_{(6)}\text{-PrO}_{2(4)}/\gamma\text{-Al}_2\text{O}_3$ has a maximum current for NH_3 oxidation, as compared to the other members of the series.

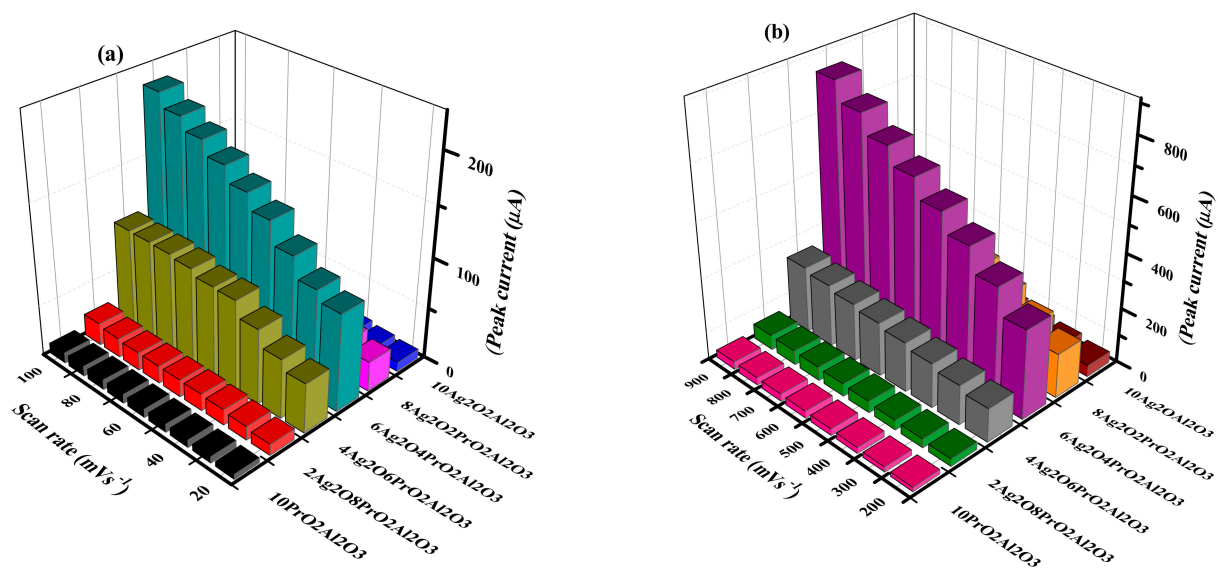


Figure 9. Comparative I_{p_a} values at modified electrodes surface on (a) low and (b) high scan.

The shift in peak potential with increasing scan rate is further confirmed by linear relationship of E_{p_a} and scan rate as shown in Figure 10b, which is one of the criteria to judge irreversibility of system [55,56]. The diffusion character of ammonia oxidation is substantiated by linear dependence of anodic peak current on scan rate, which is depicted by plots of $\ln I_{p_a}$ vs. $\ln \nu$ [55,57], as shown in Figure 10c. The slope values close to 0.5 represent diffusion-controlled electrode processes, whereas close to 1.0 will be for adsorption-controlled processes [58–60]. The behavior of current function with scan rate is also examined for oxidation of ammonia figures (Figure 10D). The current function decreases exponentially with increasing sweep rate, which is suitable for electrode process. The negative slopes from these exponential plots determine that electrochemical oxidation of ammonia on the surface of all modified electrodes is expedited and the process is electrocatalytic [61].

It is revealed from the scan rate effect for all the electrochemical systems that the current increases with the increase of scan rate, and the peak potential is shifted towards a more positive potential region.

5.2. Kinetics of Ammonia Electro-Oxidation

The diffusion character of ammonia oxidation is demonstrated by linear dependence of anodic peak current on scan rate, which is depicted by plots of $\ln I_{p_a}$ vs. $\ln \nu$ (Figure 10C). For the determination of diffusion coefficient, the Randles–Ševčík equation is used [62]:

$$I_p = (2.99 \times 10^5) \cdot n \cdot \{(1-\alpha) \cdot n_\alpha\} \cdot A \cdot D^{\circ 1/2} \cdot C \cdot \nu^{1/2} \quad (4)$$

where I_p is the anodic peak current; n is the no. of electrons involved in reaction; α is the transfer co-efficient whose value lies in the (0.3–0.7) range; n_α is the number of electrons in the rate-determining step, i.e., 3; A is area of the electrode, which is 0.07 cm^2 ; D° is the diffusion co-efficient in $\text{cm}^2 \cdot \text{s}^{-1}$; C is the bulk concentration in $\text{mol} \cdot \text{cm}^{-3}$; and ν is the scan rate in $\text{mV} \cdot \text{s}^{-1}$. The parameter α is calculated by using the following:

$$E_{p_a} - E_{p_{a/2}} = [0.048 / (\alpha n)] \quad (5)$$

where, E_{p_a} is anodic peak potential and $E_{p_{a/2}}$ is peak potential at $I_{p_{a/2}}$.

It is deduced that the reaction is diffusion controlled at low sweep rates, while it is kinetically controlled at higher scan rate (Figure 10C) [55,57].

The mass transport coefficient (m_T) is given by Equation (5) [63]:

$$m_T = [D^\circ / (RT / (F \cdot \nu))]^{1/2} \quad (6)$$

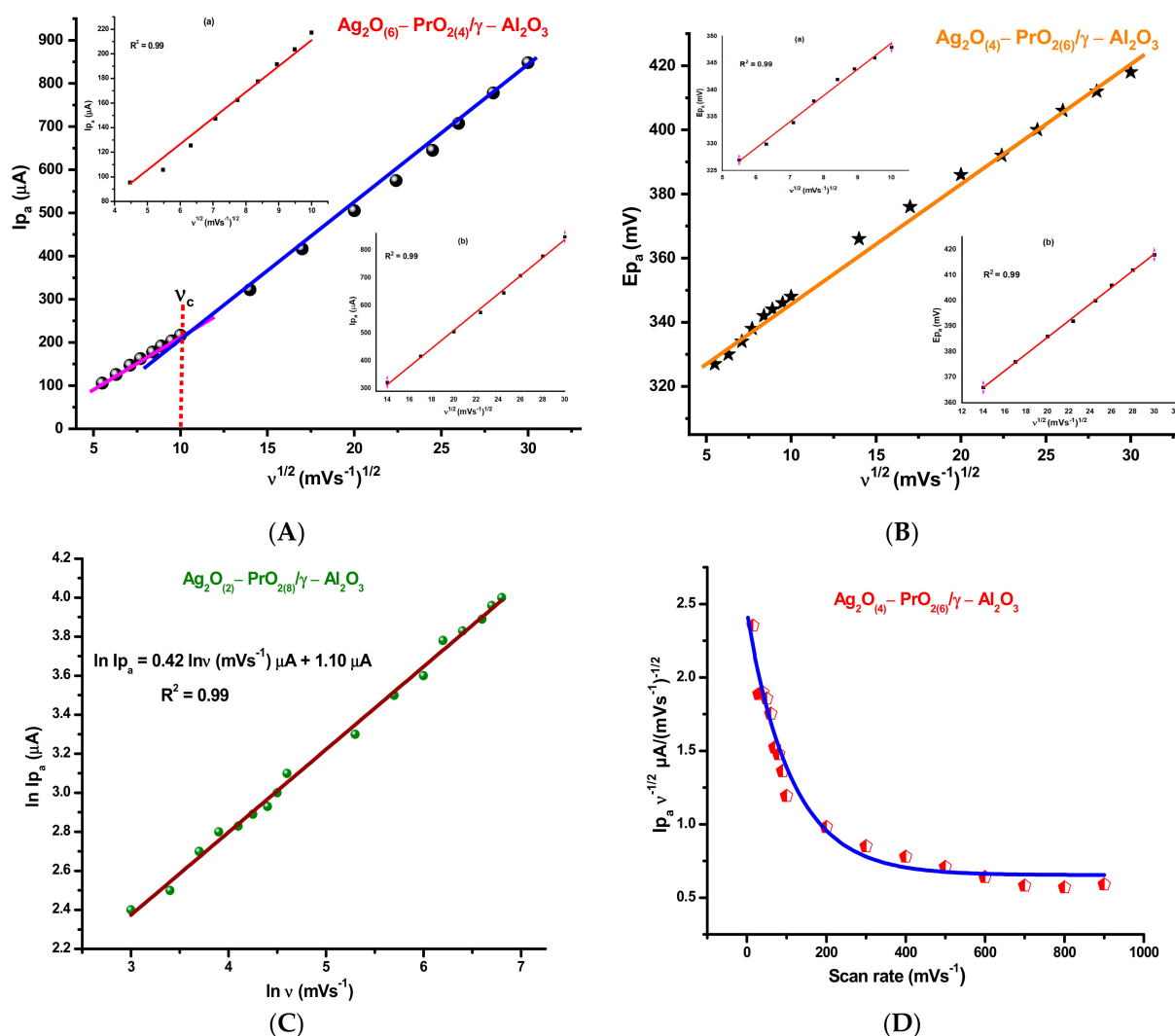


Figure 10. (A) Dependence of I_{p_a} on $v^{1/2}$; insets (a) and (b) show linear fitting for lower and higher scan rates for $\text{Ag}_2\text{O}_{(6)}-\text{PrO}_{2(4)}/\gamma-\text{Al}_2\text{O}_3/\text{GC}$. (B) Characteristic shift in peak potential with $v^{1/2}$ for $\text{Ag}_2\text{O}_{(4)}-\text{PrO}_{2(6)}/\gamma-\text{Al}_2\text{O}_3/\text{GC}$, insets (a) and (b) show linear fitting for lower and higher scan rates. (C) Dependence of I_{p_a} on potential scan rate in double logarithm coordinates for ammonia oxidation on $\text{Ag}_2\text{O}_{(2)}-\text{PrO}_{2(8)}/\gamma-\text{Al}_2\text{O}_3/\text{GC}$. (D) Variation of current function ($I_{p_a} v^{-1/2}$) with v for $\text{Ag}_2\text{O}_{(4)}-\text{PrO}_{2(6)}/\gamma-\text{Al}_2\text{O}_3/\text{GC}$.

The values of the ammonia diffusion and mass transport coefficients for the entire series of the synthesized samples are given in Table 4. The diffusion coefficient and mass transport coefficient are higher for $\text{Ag}_2\text{O}_{(6)}-\text{PrO}_{2(4)}/\gamma-\text{Al}_2\text{O}_3$, revealing that it is a better electro-active material for NH_3 oxidation among all the samples. The value of diffusion coefficients for ammonia oxidation in alkaline medium (10^{-9}) is smaller than that of H_2O (10^{-5}), due to presence of hydroxyl groups of the supporting electrolyte present in bulk [64]. These hydroxyl groups from the KOH electrolyte hinder the diffusion process of ammonia; that could be the reason for the low diffusion coefficient. The diffusion coefficient value estimated for ammonia over $\text{Ag}_2\text{O}_{(6)}-\text{PrO}_{2(4)}/\gamma-\text{Al}_2\text{O}_3$ nanocomposite seems similar to ammonia diffusion over the Pt-Ni composite [65]. Moreover, these diffusion coefficient values are obtained for the current of major peak, i.e., around 0.4 V, which increases linearly

with the scan rate, as seen from Figure 8. It suggests that oxidation of ammonia over $\text{Ag}_2\text{O}_{(6)}\text{-PrO}_{2(4)}/\gamma\text{-Al}_2\text{O}_3$ is governed by diffusion significantly.

The catalytic properties of synthesized materials can be determined by heterogeneous kinetics for ammonia oxidation. The value of heterogeneous rate constant was determined by taking cyclic voltammograms and varying the concentration of ammonia (Figure 11a). The Reinmuth equation is used to calculate heterogeneous rate constants, k° , for all supported mixed metal oxide electrocatalysts.

$$I_p = 0.227n \cdot F \cdot A \cdot C \cdot k^\circ \quad (7)$$

where k° is the heterogeneous rate constant, and F is Faraday's constant. By plotting the anodic peak current vs. concentration of NH_3 , the values of the rate constant, k° , for oxidation are obtained from the slope, as illustrated in Table 5, which reveals the facilitated electron transfer process, and it gives valuable information about the nature of system, which is irreversible. The heterogeneous rate constant decreases in the following order:

$$k^\circ_{(6\text{Ag-4Pr/Al})} > k^\circ_{(4\text{Ag-6Pr/Al})} > k^\circ_{(8\text{Ag-2Pr/Al})} > k^\circ_{(10\text{Ag/Al})} > k^\circ_{(2\text{Ag-8Pr/Al})} > k^\circ_{(10\text{Pr/Al})}$$

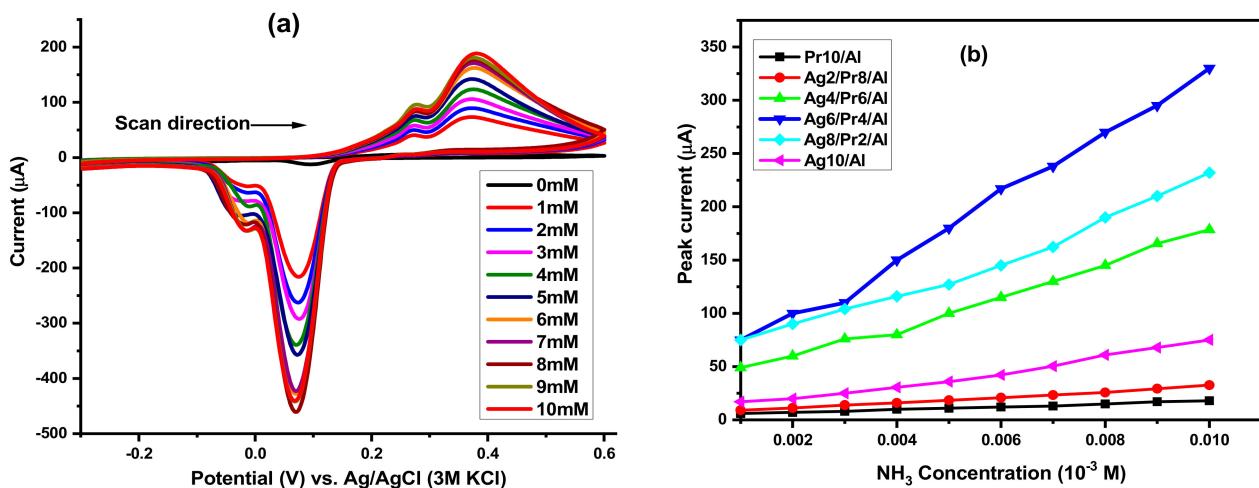


Figure 11. (a) Cyclic voltammograms with $\text{Ag}_2\text{O}_{(8)}\text{-PrO}_{2(2)}/\gamma\text{-Al}_2\text{O}_3$ electrode at different concentrations of NH_3 and (b) Reinmuth plots between I_{p_a} and C_{NH_3} , showing variation of peak current with C_{NH_3} for and for all modified electrodes.

Table 5. Kinetic parameters for NH_3 electro-oxidation at the electrode surfaces.

Electrocatalysts	α	$(D^\circ)/10^{-9}$ $\text{cm}^2 \cdot \text{s}^{-1}$	$(m\Gamma)/\text{cm} \cdot \text{s}^{-1}$	$k^\circ/10^{-3} \text{ cm} \cdot \text{s}^{-1}$
$\text{PrO}_{2(10)}/\gamma\text{-Al}_2\text{O}_3$	0.5	0.063	0.0005	0.40
$\text{Ag}_2\text{O}_{(2)}\text{-PrO}_{2(8)}/\gamma\text{-Al}_2\text{O}_3$	0.5	0.140	0.0007	0.72
$\text{Ag}_2\text{O}_{(4)}\text{-PrO}_{2(6)}/\gamma\text{-Al}_2\text{O}_3$	0.7	11.00	0.0070	6.10
$\text{Ag}_2\text{O}_{(6)}\text{-PrO}_{2(4)}/\gamma\text{-Al}_2\text{O}_3$	0.6	36.50	0.0120	7.40
$\text{Ag}_2\text{O}_{(8)}\text{-PrO}_{2(2)}/\gamma\text{-Al}_2\text{O}_3$	0.4	4.040	0.0040	5.20
$\text{Ag}_2\text{O}_{(10)}/\gamma\text{-Al}_2\text{O}_3$	0.4	0.300	0.0011	1.60

5.3. Thermodynamic Studies for Ammonia Electro-Oxidation

Cyclic voltammograms were observed by varying the temperature of the system from 10 to 50 °C with the $\text{Ag}_2\text{O}_{(6)}\text{-PrO}_{2(4)}/\gamma\text{-Al}_2\text{O}_3$ catalyst, as shown in Figure 12a. The observed thermodynamic parameters tabulated below show that electro-oxidation of ammonia in alkaline solution is exothermic and non-spontaneous reaction. The entropy of ammonia electro-oxidation is negative because it is an adsorption-controlled process. Before adsorption, the molecules are free to move in three dimensions; when these get adsorbed on the surface of catalyst, their motion is restricted. As a result, disorderliness decreases, and entropy of the system decreases. The free energy of activation is less for $\text{Ag}_2\text{O}_{(6)}\text{-PrO}_{2(4)}/\gamma\text{-Al}_2\text{O}_3$ modified electrode, which reveals that this composition exhibits superior catalytic properties among this series because it lowers the activation energy of system to a greater extent.

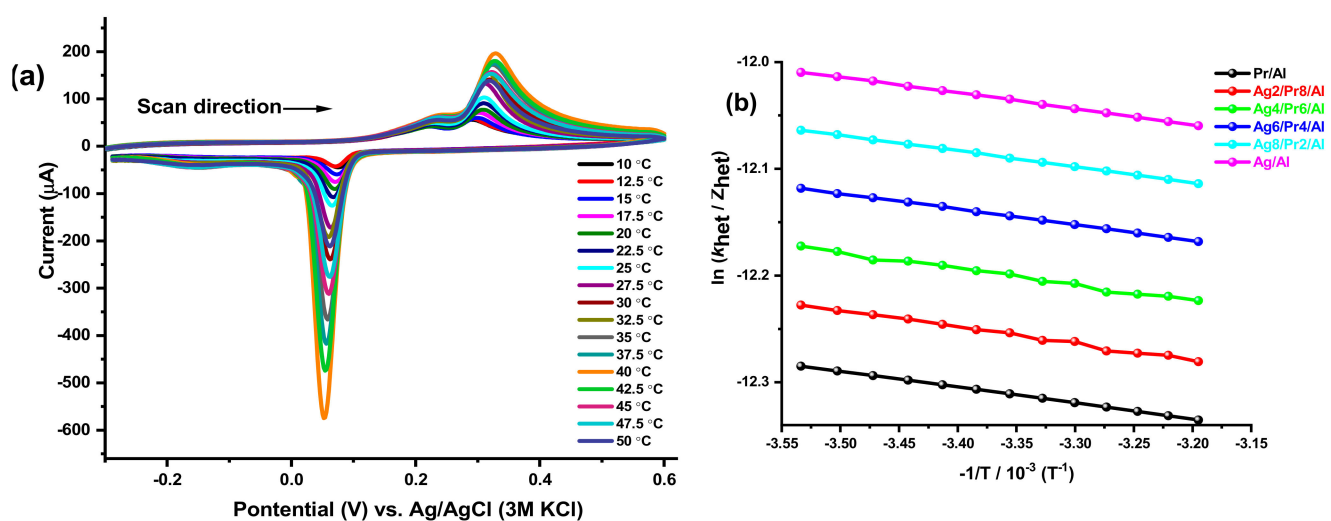


Figure 12. (a) Peak current output varied with increase in temperature and (b) Marcus plots between temperature and rate constants.

All the compositions in the series exhibit a similar response towards the increase in temperature of the system. Different thermodynamic parameters enlisted in Table 6 are deduced for the NH_3 electro-oxidation, with the help of the Marcus equation. It is a straight-line equation and gives the value of enthalpy of reaction (ΔH) from the slope of the Marcus plot, i.e., Figure 12b between $\ln [k^\circ / Z_{\text{het}}]$ vs. $-1/T$, while change in entropy (ΔS) can be estimated from the intercept.

$$k^\circ = Z_{\text{het}} \cdot \exp \left[\frac{-\Delta G}{RT} \right] \quad (8)$$

Equations (5) and (6) may be expressed in a simpler form:

$$\ln \frac{k^\circ}{Z_{\text{het}}} = \left[\frac{-\Delta G}{RT} \right] \quad (9)$$

Here, ΔG is free energy of activation, k° heterogeneous rate constant and Z_{het} is collision number whose values Z_{het} at different temperatures (T) can be calculated by Equation (9) [66].

$$Z_{\text{het}} = \sqrt{\frac{RT}{2\pi M}} \quad (10)$$

Table 6. Thermodynamic parameters calculated from the Marcus equation.

Electrocatalysts	(ΔH)/kJ·mol ⁻¹	(ΔS)/kJ·mol ⁻¹ K ⁻¹	(ΔG)/kJ·mol ⁻¹
PrO ₂₍₁₀₎ /γ-Al ₂ O ₃	-1.24	-0.119	32.0
Ag ₂ O ₍₂₎ -PrO ₂₍₈₎ /γ-Al ₂ O ₃	-1.30	-0.100	29.0
Ag ₂ O ₍₄₎ -PrO ₂₍₆₎ /γ-Al ₂ O ₃	-1.23	-0.080	23.6
Ag ₂ O ₍₆₎ -PrO ₂₍₄₎ /γ-Al ₂ O ₃	-1.22	-0.082	23.0
Ag ₂ O ₍₈₎ -PrO ₂₍₂₎ /γ-Al ₂ O ₃	-1.23	-0.085	24.0
Ag ₂ O ₍₁₀₎ /γ-Al ₂ O ₃	-1.24	-0.094	27.0

M is the molar concentration of NH₃, according to thermodynamic equation.

$$\Delta G = \Delta H - T\Delta S \quad (11)$$

$$\ln \frac{k^o}{Z(\text{het})} = -\frac{\Delta H}{RT} + \frac{\Delta S}{R} \quad (12)$$

5.4. Mechanism of Ammonia Oxidation

The independent behavior of cathodic and anodic reactions was further confirmed by comparing the linear-sweep voltammograms (LSV) with cyclic voltammogram (CV) observed for 5 mM NH₃ in 0.1 M KOH at 100 mV·s⁻¹, as represented in Figure 13. It reveals that the anodic peak (black curve) is purely for ammonia oxidation, and the cathodic peak (blue curve) is for the reduction of silver oxide into metal silver. The comparison of LSV with CV will help to propose a mechanism for ammonia oxidation on surface of electrocatalysts.

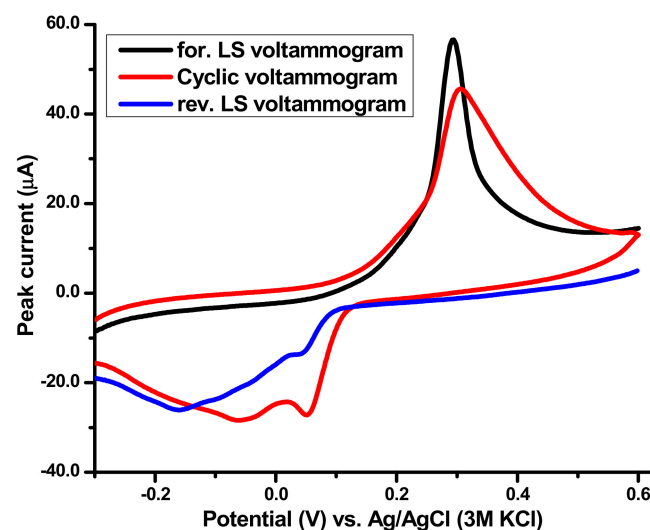
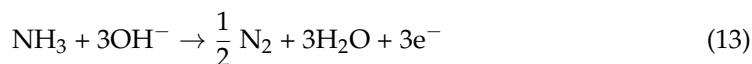


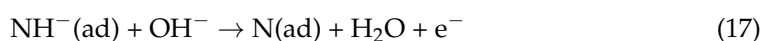
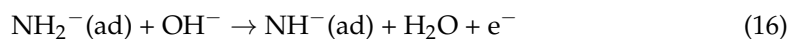
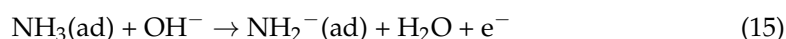
Figure 13. Linear-sweep voltammograms (LSV) vs. cyclic voltammogram (CV) for oxidation of ammonia in 0.1 M KOH at 100 mV·s⁻¹ on the surface of optimum composition/GC.

These responses correspond to the mechanism of ammonia oxidation. NH₃ is firstly adsorbed on electrode surface from bulk solution. After adsorption, it undergoes the 3e⁻ oxidation process, forming water and N₂ as by-products [67].

Overall reaction



Mechanism



6. Conclusions

The $\gamma\text{-Al}_2\text{O}_3$ supported $\text{Ag}_2\text{O}_{(x)}\text{-PrO}_{2(y)}$ nanocatalysts were synthesized via simple synthetic routes. Moreover, $\gamma\text{-Al}_2\text{O}_3$ was synthesized by precipitation method, and metal oxide promoters were loaded on $\gamma\text{-Al}_2\text{O}_3$ by co-impregnation method. All the as-synthesized materials were subjected to characterization techniques, including FTIR, XRD, EDX, SEM, CV and EIS. The sizes of the proposed nanocatalysts were calculated by XRD and SEM, which confirms that synthesized materials are in nano-range and are well dispersed on the support. The successful loading of $x\text{Ag}_2\text{O}\text{-}y\text{PrO}_2$ nanocomposites on support was confirmed by XRD, FTIR and EDX. The surface morphology of samples was examined by SEM, which shows that metal oxide precursors are homogeneously dispersed on the surface of the support. The active surface area and electron transfer constant were calculated by CV and EIS. All the compositions gave appreciable current output in ammonia electro-oxidation reaction, owing to their estimated ECSA values and electron transfer properties. Among all the catalysts in the series, $\text{Ag}_2\text{O}_{(6)}\text{-PrO}_{2(4)}/\gamma\text{-Al}_2\text{O}_3$ gave the higher values for both, making it an optimum composition for electrochemical applications.

The cyclic voltammetric investigations were employed for analyzing the electrochemical properties of materials. The catalytic activity of all synthesized samples was investigated towards oxidation of ammonia, considering scan rate, concentration and temperature effects in focus. All modified electrodes showed adequate catalytic behavior towards ammonia oxidation, whereby modified electrodes behaved as anodic material. The calculated kinetic parameters revealed that ammonia oxidation on these catalysts was of diffusion control nature and irreversible. The thermodynamic parameters declared that the overall process of ammonia on catalysts surface was exothermic (negative enthalpy) and non-spontaneous (positive Gibbs free energy). The entropy of the system was negative, as disorderliness decreases in the system due to adsorption of intermediate species on the catalyst surface before oxidation, which reveals that ammonia electro-oxidation is an adsorption-controlled process. Among all modified electrodes, the $\text{Ag}_2\text{O}_{(6)}\text{-PrO}_{2(4)}/\gamma\text{-Al}_2\text{O}_3$ modified electrode exhibited better catalytic response, owing to its higher diffusion coefficient, mass transport coefficient, heterogeneous rate constant and lowest free energy of activation.

Author Contributions: Conceptualization, M.K. and N.K.J.; Methodology, M.K. and N.K.J.; Validation, S.K.; Formal Analysis, T.S.A.; Investigation, N.K.J.; Resources, S.A.; Data Curation, N.K.J.; Writing—Original Draft Preparation, M.K.; Writing—Review and Editing, N.K.J.; Visualization, S.K.; Supervision, N.K.J.; Project Administration, N.K.J.; SEM characterization, I.Q.; TEM characterization, S.A.; Funding Acquisition, T.S.A. All authors have read and agreed to the published version of the manuscript.

Funding: This research received no external funding.

Data Availability Statement: Data is contained within article.

Acknowledgments: The authors acknowledge the Fuel Cell Lab, Department of Chemistry, Quaid-I-Azam University, Islamabad, which furnished this novel research, and the researchers collaborative Project Number (RSP-2020/254), King Saud University, Riyadh, Saudi Arabia.

Conflicts of Interest: The authors declare no conflict of interest.

References

1. Nowotny, J.; Hoshino, T.; Dodson, J.; Atanacio, A.J.; Ionescu, M.; Peterson, V.; Prince, K.E.; Yamawaki, M.; Bak, T.; Sigmund, W.; et al. Towards sustainable energy. Generation of hydrogen fuel using nuclear energy. *Int. J. Hydrogen Energy* **2016**, *41*, 12812–12825. [[CrossRef](#)]
2. Pervaiz, M.; Ahmad, I.; Yousaf, M.; Kirn, S.; Munawar, A.; Saeed, Z.; Adnan, A.; Gulzar, T.; Kamal, T.; Ahmad, A.; et al. Synthesis, spectral and antimicrobial studies of amino acid derivative Schiff base metal (Co, Mn, Cu, and Cd) complexes. *Spectrochim. Acta Part A Mol. Biomol. Spectrosc.* **2019**, *206*, 642–649. [[CrossRef](#)] [[PubMed](#)]
3. Kashif, M.; Ngaini, Z.; Harry, A.V.; Vekariya, R.L.; Ahmad, A.; Zuo, Z.; Sahari, S.K.; Hussain, S.; Khan, Z.A.; Alarifi, A. An experimental and DFT study on novel dyes incorporated with natural dyes on titanium dioxide (TiO₂) towards solar cell application. *Appl. Phys. A* **2020**, *126*, 1–13. [[CrossRef](#)]
4. Ahmad, A.; Jini, D.; Aravind, M.; Parvathiraja, C.; Ali, R.; Kiyani, M.Z.; Allothman, A. A novel study on synthesis of egg shell based activated carbon for degradation of methylene blue via photocatalysis. *Arab. J. Chem.* **2020**, *13*, 8717–8722. [[CrossRef](#)]
5. Hussain, S.; Khan, A.J.; Arshad, M.; Javed, M.S.; Ahmad, A.; Shah, S.S.A.; Khan, M.R.; Akram, S.; Zulfiqar, Ali, S.; et al. Charge storage in binder-free 2D-hexagonal CoMoO₄ nanosheets as a redox active material for pseudocapacitors. *Ceram. Int.* **2020**. [[CrossRef](#)]
6. Afif, A.; Radenahmad, N.; Cheok, Q.; Shams, S.; Kim, J.H.; Azad, A.K. Ammonia-fed fuel cells: A comprehensive review. *Renew. Sustain. Energy Rev.* **2016**, *60*, 822–835. [[CrossRef](#)]
7. Zhang, X.Z.; Xu, P.H.; Liu, G.W.; Ahmad, A.; Chen, X.H.; Zhu, Y.L.; Allothman, A.; Hussain, S.; Qiao, G.J. Synthesis, Characterization and Wettability of Cu-Sn Alloy on the Si-Implanted 6H-SiC. *Coatings* **2020**, *10*, 906. [[CrossRef](#)]
8. Aravind, M.; Ahmad, A.; Ahmad, I.; Amalanathan, M.; Naseem, K.; Mary, S.M.M.; Parvathiraja, C.; Hussain, S.; Algarni, T.S.; Pervaiz, M.; et al. Critical green routing synthesis of silver NPs using jasmine flower extract for biological activities and photocatalytic degradation of methylene blue. *J. Environ. Chem. Eng.* **2021**, *9*, 104877. [[CrossRef](#)]
9. Naseem, K.; Rehman, M.Z.U.; Ahmad, A.; Dubal, D.; Algarni, T.S. Plant Extract Induced Biogenic Preparation of Silver Nanoparticles and Their Potential as Catalyst for Degradation of Toxic Dyes. *Coatings* **2020**, *10*, 1235. [[CrossRef](#)]
10. Zhan, M.; Hussain, S.; Algarni, T.S.; Shah, S.; Liu, J.; Zhang, X.; Ahmad, A.; Javed, M.S.; Qiao, G.; Liu, G. Facet controlled polyhedral ZIF-8 MOF nanostructures for excellent NO₂ gas-sensing applications. *Mater. Res. Bull.* **2021**, *136*, 111133. [[CrossRef](#)]
11. Khan, F.S.A.; Mubarak, N.M.; Khalid, M.; Walvekar, R.; Abdullah, E.C.; Ahmad, A.; Karri, R.R.; Pakalapati, H. Functionalized multi-walled carbon nanotubes and hydroxyapatite nanorods reinforced with polypropylene for biomedical application. *Sci. Rep.* **2021**, *11*, 1–10. [[CrossRef](#)] [[PubMed](#)]
12. Kashif, M.; Jafaar, E.; Sahari, S.K.; Low, F.W.; Hoa, N.D.; Ahmad, A.; Abbas, A.; Ngaini, Z.; Shafa, M.; Qurashi, A. Organic sensitization of graphene oxide and reduced graphene oxide thin films for photovoltaic applications. *Int. J. Energy Res.* **2021**. [[CrossRef](#)]
13. Vidal-Iglesias, F.J.; Solla-Gullón, J.; Montiel, V.; Feliu, J.; Aldaz, A. Screening of electrocatalysts for direct ammonia fuel cell: Ammonia oxidation on PtMe (Me: Ir, Rh, Pd, Ru) and preferentially oriented Pt(100) nanoparticles. *J. Power Sources* **2007**, *171*, 448–456. [[CrossRef](#)]
14. Thou, C.Z.; Khan, F.S.A.; Mubarak, N.; Ahmad, A.; Khalid, M.; Jagadish, P.; Walvekar, R.; Abdullah, E.; Khan, S.; Khan, M.; et al. Surface charge on chitosan/cellulose nanowhiskers composite via functionalized and untreated carbon nanotube. *Arab. J. Chem.* **2021**, *14*, 103022. [[CrossRef](#)]
15. Saleem, M.; Irfan, M.; Tabassum, S.; Albaqami, M.D.; Javed, M.S.; Hussain, S.; Pervaiz, M.; Ahmad, I.; Ahmad, A.; Zuber, M. Experimental and theoretical study of highly porous lignocellulose assisted metal oxide photoelectrodes for dye-sensitized solar cells. *Arab. J. Chem.* **2021**, *14*, 102937. [[CrossRef](#)]
16. Zou, P.; Chen, S.; Lan, R.; Tao, S. Investigation of Perovskite Oxide SrCo_{0.8}Cu_{0.1}Nb_{0.1}O_{3-δ} as a Cathode Material for Room Temperature Direct Ammonia Fuel Cells. *ChemSusChem* **2019**, *12*, 2788–2794. [[CrossRef](#)]
17. Adli, N.M.; Zhang, H.; Mukherjee, S.; Wu, G. Review—Ammonia Oxidation Electrocatalysis for Hydrogen Generation and Fuel Cells. *J. Electrochem. Soc.* **2018**, *165*, J3130–J3147. [[CrossRef](#)]
18. Suzuki, S.; Muroyama, H.; Matsui, T.; Eguchi, K. Fundamental studies on direct ammonia fuel cell employing anion exchange membrane. *J. Power Sources* **2012**, *208*, 257–262. [[CrossRef](#)]
19. Li, L.; Zhu, Z.; Yan, Z.; Lu, G.; Rintoul, L. Catalytic ammonia decomposition over Ru/carbon catalysts: The importance of the structure of carbon support. *Appl. Catal. A: Gen.* **2007**, *320*, 166–172. [[CrossRef](#)]
20. Schaper, H.; Doesburg, E.; Van Reijen, L. The influence of lanthanum oxide on the thermal stability of gamma alumina catalyst supports. *Appl. Catal.* **1983**, *7*, 211–220. [[CrossRef](#)]
21. Mardkhe, M.K.; Huang, B.; Bartholomew, C.H.; Alam, T.M.; Woodfield, B.F. Synthesis and characterization of silica doped alumina catalyst support with superior thermal stability and unique pore properties. *J. Porous Mater.* **2015**, *23*, 475–487. [[CrossRef](#)]
22. Jo, J.-O.; Trinh, Q.H.; Kim, S.H.; Mok, Y.S. Plasma-catalytic decomposition of nitrous oxide over γ-alumina-supported metal oxides. *Catal. Today* **2018**, *310*, 42–48. [[CrossRef](#)]
23. Yang, X.; Sun, M.; Liu, B.; Lin, W. NO_x removal by oxidation on alumina supported metal oxide catalysts followed by alkaline absorption. *China Pet. Process. Petrochem. Technol.* **2019**, *21*, 1–9.

24. Sandupatla, A.S.; Ray, K.; Thaosan, P.; Sivananda, C.; Deo, G. Oxidative dehydrogenation of propane over alumina supported vanadia catalyst—Effect of carbon dioxide and secondary surface metal oxide additive. *Catal. Today* **2020**, *354*, 176–182. [[CrossRef](#)]
25. Adil, S.F.; Assal, M.E.; Khan, M.; Shaik, M.R.; Kuniyil, M.; Sekou, D.; Dewidar, A.Z.; Al-Warthan, A.; Siddiqui, M.R.H. Eco-Friendly Mechanochemical Preparation of Ag₂O–MnO₂/Graphene Oxide Nanocomposite: An Efficient and Reusable Catalyst for the Base-Free, Aerial Oxidation of Alcohols. *Catalysts* **2020**, *10*, 281. [[CrossRef](#)]
26. Yin, Z.; Xie, L.; Cao, S.; Xiao, Y.; Chen, G.; Jiang, Y.; Wei, W.; Wu, L. Ag/Ag₂O confined visible-light driven catalyst for highly efficient selective hydrogenation of nitroarenes in pure water medium at room temperature. *Chem. Eng. J.* **2020**, *394*, 125036. [[CrossRef](#)]
27. Tankov, I.; Arishtirova, K.; Bueno, J.M.; Damyanova, S. Surface and structural features of Pt/PrO₂–Al₂O₃ catalysts for dry methane reforming. *Appl. Catal. A: Gen.* **2014**, *474*, 135–148. [[CrossRef](#)]
28. Wachs, I.E. Recent conceptual advances in the catalysis science of mixed metal oxide catalytic materials. *Catal. Today* **2005**, *100*, 79–94. [[CrossRef](#)]
29. Sharma, R.V.; Kumar, P.; Dalai, A.K. Selective hydrogenolysis of glycerol to propylene glycol by using Cu:Zn:Cr:Zr mixed metal oxides catalyst. *Appl. Catal. A Gen.* **2014**, *477*, 147–156. [[CrossRef](#)]
30. Berenguer Betrián, R.; Quijada, C.; Morallón, E. The nature of the electro-catalytic response of mixed metal oxides: Pt-and Ru-doped SnO₂ anodes. *ChemElectroChem* **2019**, *6*, 1057–1068. [[CrossRef](#)]
31. Gangwar, J.; Gupta, B.K.; Kumar, P.; Tripathi, S.K.; Srivastava, A.K. Time-resolved and photoluminescence spectroscopy of θ -Al₂O₃ nanowires for promising fast optical sensor applications. *Dalton Trans.* **2014**, *43*, 17034–17043. [[CrossRef](#)] [[PubMed](#)]
32. Domínguez-Crespo, M.; Díaz-García, L.; De La Paz, M.C.; Zárate-Ramos, R.; Santes, V.; Pérez, G.L.; Arce-Estrada, E.; Torres-Huerta, A. Influence of Alumina Crystal Size on the Hydrotreating Activity of Supported NiMo Catalysts Using Real Feedstock. *Pet. Sci. Technol.* **2006**, *24*, 485–506. [[CrossRef](#)]
33. Xu, L.; Wei, B.; Liu, W.; Zhang, H.; Su, C.; Che, J. Flower-like ZnO–Ag₂O composites: Precipitation synthesis and photocatalytic activity. *Nanoscale Res. Lett.* **2013**, *8*, 536. [[CrossRef](#)]
34. Zhu, L.; Wei, B.; Xu, L.; Lu, Z.; Zhang, H.; Gao, H.; Che, J. Ag₂O–Bi₂O₃ composites: Synthesis, characterization and high efficient photocatalytic activities. *CrystEngComm* **2012**, *14*, 5705–5709. [[CrossRef](#)]
35. Dhoondia, Z.H.; Chakraborty, H. Lactobacillus mediated synthesis of silver oxide nanoparticles. *Nanomater. Nanotechnol.* **2012**, *2*, 15. [[CrossRef](#)]
36. Vorokh, A. Scherrer formula: Estimation of error in determining small nanoparticle size. *Nanosyst. Physics, Chem. Math.* **2018**, *9*. [[CrossRef](#)]
37. Ghosh, M.; Dilawar, N.; Bandyopadhyay, A.K.; Raychaudhuri, A.K. Phonon dynamics of Zn(Mg,Cd)O alloy nanostructures and their phase segregation. *J. Appl. Phys.* **2009**, *106*, 084306. [[CrossRef](#)]
38. Mahan, G.D.; Lucas, A.A. Collective vibrational modes of adsorbed CO. *J. Chem. Phys.* **1978**, *68*, 1344–1348. [[CrossRef](#)]
39. Cheng, B.; Xiao, Y.; Wu, G.; Zhang, L. The vibrational properties of one-dimensional ZnO: Ce nanostructures. *Appl. Phys. Lett.* **2004**, *84*, 416–418. [[CrossRef](#)]
40. Tripathi, S.; Mehrotra, G.K.; Dutta, P.K. Chitosan–silver oxide nanocomposite film: Preparation and antimicrobial activity. *Bull. Mater. Sci.* **2011**, *34*, 29–35. [[CrossRef](#)]
41. Waterhouse, G.I.N.; Bowmaker, G.A.; Metson, J.B. The thermal decomposition of silver (I, III) oxide: A combined XRD, FT-IR and Raman spectroscopic study. *Phys. Chem. Chem. Phys.* **2001**, *3*, 3838–3845. [[CrossRef](#)]
42. González Hernández, N.N.; Contreras, J.L.; Pinto, M.; Zeifert, B.; Flores Moreno, J.L.; Fuentes, G.A.; Hernández-Terán, M.E.; Vázquez, T.; Salmones, J.; Jurado, J.M. Improved NO_x reduction using C₃H₈ and H₂ with Ag/Al₂O₃ catalysts promoted with Pt and WO_x. *Catalysts* **2020**, *10*, 1212. [[CrossRef](#)]
43. Yiğitalp, A. Nafion Modified NCA Cathode Synthesis for Superior Cycling Performance of Lithium-Ion Batteries. Ph.D. Thesis, Sabancı University, Istanbul, Turkey, 2019.
44. Kashif, M.; Jaafar, E.; Bhadja, P.; Low, F.W.; Sahari, S.K.; Hussain, S.; Loong, F.K.; Ahmad, A.; Algarni, T.S.; Shafa, M.; et al. Effect of potassium permanganate on morphological, structural and electro-optical properties of graphene oxide thin films. *Arab. J. Chem.* **2021**, *14*, 102953. [[CrossRef](#)]
45. Sharifi, E.; Salimi, A.; Shams, E. Electrocatalytic activity of nickel oxide nanoparticles as mediatorless system for NADH and ethanol sensing at physiological pH solution. *Biosens. Bioelectron.* **2013**, *45*, 260–266. [[CrossRef](#)]
46. Sharifi, E.; Salimi, A.; Shams, E.; Noorbakhsh, A.; Amini, M.K. Shape-dependent electron transfer kinetics and catalytic activity of NiO nanoparticles immobilized onto DNA modified electrode: Fabrication of highly sensitive enzymeless glucose sensor. *Biosens. Bioelectron.* **2014**, *56*, 313–319. [[CrossRef](#)]
47. Guo, D.J.; Li, H.L. Highly dispersed Ag nanoparticles on functional MWNT surfaces for methanol oxidation in alkaline solution. *Carbon* **2005**, *43*, 1259–1264. [[CrossRef](#)]
48. Droog, J.M.; Huisman, F. Electrochemical formation and reduction of silver oxides in alkaline media. *J. Electroanal. Chem.* **1980**, *115*, 211–224. [[CrossRef](#)]
49. Sun, Z.; Han, Y.; Gao, M.; Wei, X.; Hu, X. Cetyl trimethyl ammonium bromide-assisted electrochemical preparation of palladium-nickel bimetallic electrode. *Int. J. Electrochem. Sci.* **2011**, *6*, 5626–5638.

50. Matinise, N.; Mayedwa, N.; Ikpo, C.O.; Hlongwa, N.W.; Ndipingwi, M.M.; Molefe, L.; Dywili, N.; Yonkeu, A.L.D.; Waryo, T.; Baker, P.G.L.; et al. Bimetallic Nanocomposites of Palladium (100) and Ruthenium for Electrooxidation of Ammonia. *J. Nano Res.* **2016**, *44*, 100–113. [[CrossRef](#)]
51. Lomocso, T.L.; Baranova, E.A. Electrochemical oxidation of ammonia on carbon-supported bi-metallic PtM (M=Ir, Pd, SnOx) nanoparticles. *Electrochim. Acta* **2011**, *56*, 8551–8558. [[CrossRef](#)]
52. Matsui, T.; Suzuki, S.; Katayama, Y.; Yamauchi, K.; Okanishi, T.; Muroyama, H.; Eguchi, K. In Situ Attenuated Total Reflection Infrared Spectroscopy on Electrochemical Ammonia Oxidation over Pt Electrode in Alkaline Aqueous Solutions. *Langmuir* **2015**, *31*, 11717–11723. [[CrossRef](#)]
53. Katayama, Y.; Okanishi, T.; Muroyama, H.; Matsui, T.; Eguchi, K. Electrochemical oxidation of ammonia over rare earth oxide modified platinum catalysts. *J. Phys. Chem. C* **2015**, *119*, 9134–9141. [[CrossRef](#)]
54. Zhang, H.; Wang, Y.; Wu, Z.; Leung, D.Y. An ammonia electrolytic cell with NiCu/C as anode catalyst for hydrogen production. *Energy Procedia* **2017**, *142*, 1539–1544. [[CrossRef](#)]
55. Chrzescijanska, E.; Wudarska, E.; Kusmierek, E.; Rynkowski, J. Study of acetylsalicylic acid electroreduction behavior at platinum electrode. *J. Electroanal. Chem.* **2014**, *713*, 17–21. [[CrossRef](#)]
56. Mujtaba, A.; Janjua, N.K. Fabrication and electrocatalytic application of CuO@Al₂O₃ hybrids. *J. Electrochem. Soc.* **2015**, *162*, H328. [[CrossRef](#)]
57. Castilho, M.; Almeida, L.E.; Tabak, M.; Mazo, L.H. Voltammetric oxidation of dipyrindamole in aqueous acid solutions. *J. Braz. Chem. Soc.* **2000**, *11*, 148–153. [[CrossRef](#)]
58. Holze, R.; Brett, C.M.A.; Brett, A.M.O. *Electrochemistry—Principles, Methods and Applications*; Oxford University Press Inc.: New York, NY, USA, 1993.
59. Soleymani, J.; Hasanzadeh, M.; Shadjou, N.; Jafari, M.K.; Gharamaleki, J.V.; Yadollahi, M.; Jouyban, A. A new kinetic–mechanistic approach to elucidate electrooxidation of doxorubicin hydrochloride in unprocessed human fluids using magnetic graphene based nanocomposite modified glassy carbon electrode. *Mater. Sci. Eng. C* **2016**, *61*, 638–650. [[CrossRef](#)]
60. Masek, A.; Chrzescijanska, E.; Zaborski, M. Electrooxidation of morin hydrate at a Pt electrode studied by cyclic voltammetry. *Food Chem.* **2014**, *148*, 18–23. [[CrossRef](#)] [[PubMed](#)]
61. Mazloum-Ardakani, M.; Taleat, Z. Investigation of electrochemistry behavior of hydroxylamine at glassy carbon electrode by indigocarmin. *Int. J. Electrochem. Sci.* **2009**, *4*, 694–706.
62. Janjua, N.K.; Jabeen, M.; Islam, M.; Yaqub, A.; Sabahat, S.; Mehmood, S.; Abbas, G. Electrochemical properties of barium cerate doped with zinc for methanol oxidation. *J. Chem. Soc. Pak.* **2015**, *37*.
63. Mu, Y.; Jia, D.; He, Y.; Miao, Y.; Wu, H.-L. Nano nickel oxide modified non-enzymatic glucose sensors with enhanced sensitivity through an electrochemical process strategy at high potential. *Biosens. Bioelectron.* **2011**, *26*, 2948–2952. [[CrossRef](#)] [[PubMed](#)]
64. Kapalka, A.; Cally, A.; Neodo, S.; Comminellis, C.; Wächter, M.; Udert, K.M. Electrochemical behavior of ammonia at Ni/Ni(OH)₂ electrode. *Electrochem. Commun.* **2010**, *12*, 18–21. [[CrossRef](#)]
65. Diaz, L.A.; Valenzuela-Muñiz, A.; Muthuvel, M.; Botte, G.G. Analysis of ammonia electro-oxidation kinetics using a rotating disk electrode. *Electrochim. Acta* **2013**, *89*, 413–421. [[CrossRef](#)]
66. Marcus, R.A. On the Theory of Electron-Transfer Reactions. VI. Unified Treatment for Homogeneous and Electrode Reactions. *J. Chem. Phys.* **1965**, *43*, 679–701. [[CrossRef](#)]
67. Oswin, H.G.; Salomon, M. The anodic oxidation of ammonia at platinum black electrodes in aqueous koh electrolyte. *Can. J. Chem.* **1963**, *41*, 1686–1694. [[CrossRef](#)]